Geophysical Research Letters

RESEARCH LETTER
10.1029/2019GL085705

Elevated Seismic Hazard in Kansas Due to High-Volume Injections in Oklahoma

Guang Zhai[1,2,3], Manoochehr Shirzaei[1], and Michael Manga[2,3]

[1]School of Earth and Space Exploration, Arizona State University, Tempe, AZ, USA, [2]Department of Earth and Planetary Science, University of California, Berkeley, CA, USA, [3]Berkeley Seismological Laboratory, University of California, Berkeley, CA, USA

Key Points:
- Unified hydromechanical model to reproduce and forecast induced seismicity for western Oklahoma and southern Kansas
- The state of stress and seismicity rate in Kansas are modulated by injection in Oklahoma
- The probability of large earthquakes in Kansas is exacerbated by the hydromechanical interaction with fluid injection in Oklahoma

Supporting Information:
- Supporting Information S1

Correspondence to:
G. Zhai,
gzhai@seismo.berkeley.edu

Citation:
Zhai, G., Shirzaei, M., & Manga, M. (2020). Elevated seismic hazard in Kansas due to high-volume injections in Oklahoma. *Geophysical Research Letters*, *47*, e2019GL085705. https://doi.org/10.1029/2019GL085705

Received 4 OCT 2019
Accepted 25 FEB 2020
Accepted article online 29 FEB 2020

Abstract Induced seismicity has expanded into south-central Kansas, an area with rare damaging natural earthquakes, leading to the second-highest seismicity rate in the central United States after Oklahoma. Here we assess the mechanical effects of large-scale injection in the combined area of western Oklahoma and southern Kansas during 2010–2018 and its link to the observed seismicity using physics-based hydromechanical and seismicity rate models. Such models link injection operations to seismic hazards and allow solving for the spatially variable distribution of background seismic productivity that yields an acceptable match between the observed and modeled seismicity. We show that injection in Oklahoma amplifies the total Coulomb stress change and seismicity rate by 1.5-fold and threefold, respectively, in south-central Kansas. This cross-border interaction modulates the annual earthquake probability in Kansas. We conclude that the issue of induced seismicity is not a local problem due to the far-reaching effects of fluid diffusion.

1. Introduction

A large body of evidence suggests that the sharp increase in the number of earthquakes in the eastern and central United States over the past decade is linked to the large volume of deep waste fluid disposal (Ellsworth, 2013; Rubinstein & Mahani, 2015). States experiencing the issue of induced seismicity include Oklahoma (Keranen et al., 2014), Texas (Frohlich, 2012), Colorado (Ake et al., 2005; Block et al., 2014; Yeck et al., 2014; Yeck et al., 2016), Arkansas (Horton, 2012), Ohio (Kim, 2013), New Mexico (Rubinstein et al., 2014), and California (Goebel et al., 2016). This issue has extended to Kansas, an area with a low risk of damaging natural earthquakes with a historical average of one M3.0+ earthquake every 1 to 2years (Peterie et al., 2018; Rubinstein et al., 2018). The rapid increase of seismicity since 2014 in south-central Kansas correlates with the regional growth of fluid injection into the Cambrian-Ordovician Arbuckle Group (Peterie et al., 2018). This seismic activity makes Kansas the state with the second-highest seismicity rate in the central United States. The Milan M_w4.9 earthquake in 2014 highlights the elevated seismic hazard in Kansas due to fluid injection (Choy et al., 2016; Hearn et al., 2018).

The underlying mechanism of injection-induced seismicity is well known. Fluid injected into the disposal formation diffuses in the medium and increases the pore pressure and creates poroelastic stresses, reducing frictional strength on faults and bringing them closer to failure (Healy et al., 1968; Raleigh et al., 1976). Although direct observation of subsurface pressure change is limited, this mechanism is supported by numerical simulations (Fan et al., 2016; Keranen et al., 2014; Shirzaei et al., 2016). Monitoring of Arbuckle formation pressure provides strong evidence linking the fluid injection and induced seismicity within the U.S. midcontinent through pore pressure changes (Ansari et al., 2019; Barbour et al., 2019; Kroll et al., 2017; Peterie et al., 2018). However, the relationship between fluid injection and pore pressure evolution is complex in time and space (Zhai et al., 2019; Zhai & Shirzaei, 2018). The spatiotemporal evolution of pore pressure and poroelastic stresses depends on several factors including the location, depth, and volume of injection wells as well as hydrogeological properties of the permeable reservoir (Zhai et al., 2019; Zhai & Shirzaei, 2018), which can be estimated using seismic and geodetic observations (Shirzaei et al., 2019).

Peterie et al. (2018) investigated bottom-hole pressure data in southern Kansas and showed that starting in 2011, formation pressures begin to increase suddenly despite the near-steady rate of injection. They also

noticed a northward propagation of seismicity. These observations suggest that the pressure rise may not be solely due to local injection and may be influenced by fluid migration from the distant, high-volume injection wells located near the Oklahoma-Kansas border region, nearly 90 km away (Peterie et al., 2018). Kansas thus provides an opportunity for studying the impact of distant fluid injection on regional induced seismicity.

Previous studies have focused on the pore pressure and poroelastic stress perturbations within 40 km of injection wells, resolving the first-order correlation between pore pressure and stress changes and the occurrence of isolated earthquake swarms or sequences (Goebel et al., 2017; Keranen et al., 2014). However, a quantitative study of the impact of distant injections on the local induced seismic hazard is needed. Here, we compile the injection, seismicity, and hydrogeological data for the combined area of western Oklahoma and southern Kansas during 2010–2018. We apply a physics-based induced seismicity forecasting framework to construct a unified hydromechanical model to simulate the seismicity rate within the study area caused by fluid injection. Using this model, we evaluate the impact of the far-field injections in western Oklahoma on seismic hazard in south-central Kansas.

2. Data Sets

2.1. Fluid Injection

We compile reported wastewater injection data for 668 Class II injection wells within western Oklahoma and southern Kansas, distributed by the Oklahoma Corporation Commission and the Kansas Corporation Commission. A large amount of saltwater, coproduced from oil and gas production, was injected into the Cambrian-Ordovician Arbuckle formation during 2010–2018 with a total volume of 5.87×10^8 m^3. Figure 1a shows the Arbuckle well locations, with 325 and 343 wells within Oklahoma and Kansas, respectively. The injection rate shows substantial spatiotemporal variability (Figures 1a and 1b). Note that most high-volume injection wells are within Oklahoma rather than Kansas (Figure 1a). The total injection volume in Oklahoma is ~2.8 times that in Kansas for the period of 2010–2018, while that value is ~3.3 for 2014–2016, during which seismicity peaks in Kansas (Figure 1b). The injection rate starts to increase in 2012 and peaks in early 2015. It then decreases to a level determined by the injection reduction plan in response to increased seismicity in both Oklahoma and Kansas. The coincidence of injection and seismicity increase suggests a causal link (Peterie et al., 2018).

We note that the injection volume is reported monthly in Oklahoma, while that in Kansas before 2015 is accessible online as yearly. To construct a unified hydrogeological model due to fluid injection within the combined region, as a first-order approximation, we calculate the average monthly injection rate from the yearly reported values in Kansas during 2010–2014.

2.2. Seismicity

The seismicity catalogs are obtained from the Kansas Geological Survey (KGS) and Oklahoma Geological Survey (OGS) from 2010 to 2018. Both Kansas Geological Survey and Oklahoma Geological Survey catalogs have the same magnitude of completeness of ~M2.0 (Supporting Information Figure S2). Despite the fact that different earthquake catalogs may use different magnitude scales, the empirical scaling indicates that such differences are small (Al-Ismail et al., 2019).

The recorded seismicity contains both injection-induced earthquakes as well as their aftershocks. To focus on earthquakes linked directly to injection operations, we use the algorithm of Reasenberg (1985) for earthquake catalog declustering to remove dependent earthquakes (Figure S1). Due to the spatial proximity of Kansas and Oklahoma, the parameters associated with the declustering algorithm are chosen following the previous study of induced seismicity in Oklahoma (Zhai et al., 2019). The declustering procedure reduces the total earthquake counts and seismic moment in Kansas and Oklahoma by ~63% and 40%, respectively, but the earthquake magnitude of completeness remains unchanged and is ~ M2.0 (Figures S2). Thus, we only use declustered M2.0+ earthquakes for further analysis. In Kansas, most induced earthquakes occur within the south-central region (Peterie et al., 2018). Figure 1c shows the distribution of declustered seismicity in this region with a focus on Sumner and Harper counties. Noteworthy, during the study period is the 2014 M_w4.9 Milan earthquake.

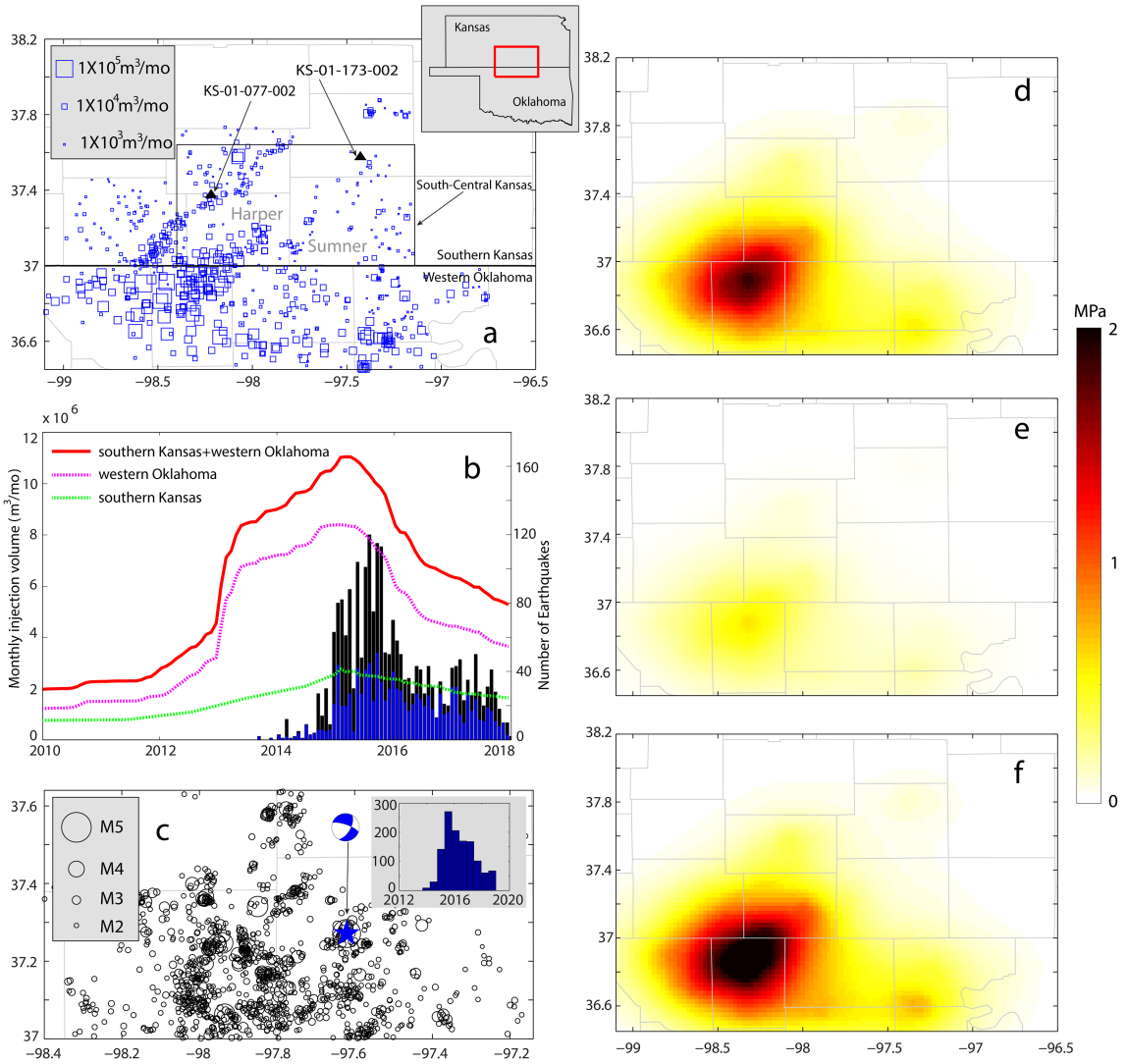

Figure 1. (a) Spatial distribution of Class II injection wells (blue squares) scaled with average monthly injection volume. Black triangles indicate the two Class I well locations that monitor bottom-hole pressure. Black rectangle indicates the area of south-central Kansas. Red rectangle in the inset shows the combined area of western Oklahoma and southern Kansas. (b) Time series of monthly M2+ earthquake number (black: original catalog from Oklahoma and Kansas Geological Survey; and blue: declustered catalog) in south-central Kansas and monthly injection volume for southern Kansas wells, western Oklahoma wells, and their addition. Kansas injection time series prior to 2015 is downsampled and reported as annual averages. (c) Spatial distribution of declustered M2+ earthquakes in south-central Kansas. Blue star shows the 2014 Milan Mw4.9 earthquake. Inset shows semiannual number of declustered M2+ earthquakes within south-central Kansas. (d) Distribution of pore pressure change scaled with friction coefficient (Table S2) during 2010–2018. (e) Coulomb stress change due to poroelastic stresses during 2010–2018. (f) Total Coulomb stress change due to both pore pressure change and poroelastic stress change. The detailed spatial and temporal evolution of pore pressure and poroelastic stress is shown in Figures S5 and S6.

3. Hydromechanical and Seismicity Rate Models

To establish the link between injection operations and seismicity, we use a physics-based induced earthquake forecasting framework, which has been used to investigate induced seismicity in Texas and Oklahoma and to evaluate the time-dependent seismic hazards due to fluid injection (Zhai et al., 2019; Zhai & Shirzaei, 2018). In this approach, the process of fluid diffusion in a poroelastic medium is linked to the mechanism of earthquake nucleation on a prestressed fault.

3.1. Hydromechanical Model

Based on the regional hydrogeological setting within the combined area of western Oklahoma and southern Kansas, we set up a poroelastic Earth model with four significant layers, including a shallow aquifer, shale,

the Arbuckle formation, and a granite basement (Text S1 and Figure S3). Each layer is characterized by five hydrogeological parameters shown in Table S1. The associated parameter values are constrained based on rock properties (Perilla-Castillo, 2017; Wang, 2000), seismic velocity (Chen, 2016; Christensen, 1996), and seismicity migration (Peterie et al., 2018). The relative distance between injection depth and the basement interface is a crucial factor controlling induced seismicity (Hincks et al., 2018) and is calculated using Arbuckle well log, depth, and isopach information (Campbell & Weber, 2006; Franseen et al., 2004; Franseen & Byrnes, 2012). The unified, curved Arbuckle-basement interface within Oklahoma and Kansas is approximated using a polynomial function (Figure S4). The relative distance between injection well-bottom depth and basement interface is used to determine the injection depth within the layered poroelastic model (Figure S3). We use the numerical solution provided by Wang and Kümpel (2003) to simulate the spatial and temporal evolution of poroelastic stresses and pore pressure due to fluid injected into the isotropic, layered poroelastic half-space. Since we use a linear poroelastic model, we can superimpose the solutions from all injection wells. Considering that the basement faults penetrate into the overlying permeable Arbuckle formation (Kolawole et al., 2019) and host fast fluid flow (Chang & Yoon, 2018; Hearn et al., 2018; Scibek et al., 2016), we estimate the changes of pore pressure and poroelastic stresses due to fluid injection at the Arbuckle-basement boundary. More information is provided in Text S1.

3.2. Earthquake Nucleation Model

We employ a rate-and-state earthquake nucleation model to simulate the evolution of seismicity rate along faults in response to Coulomb stress changes (Dieterich, 1994; Heimisson & Segall, 2018; Segall & Lu, 2015). This model calculates the expected number of earthquakes relative to the background rate as a function of time due to stress perturbations on a given fault:

$$\frac{dR}{dt} = \frac{R}{t_a}\left(\frac{\dot{\tau}}{\dot{\tau}_0} - R\right), \tag{1}$$

where R is the seismicity rate relative to the background rate; $\dot{\tau}_0$ is the background stressing rate; $t_a = \frac{A\overline{\sigma}}{\dot{\tau}_0}$ is the characteristic relaxation time; A is a constitutive parameter in the rate-and-state-dependent friction law (Dieterich, 1994); $\overline{\sigma}$ is the background effective normal stress; and $\dot{\tau}$ is the Coulomb stressing rate time series. In addition, we include a critical time t_{crit} to account for the Arbuckle pressure deficit prior to the observed seismicity increase following Zhai et al. (2019).

The Coulomb stressing rate is computed using the stress and fluid pressure from the poroelastic model, which are spatially and temporally variable (see section 3.1). To calculate the normal and shear components of the stress tensor on faults, we use a receiver fault geometry consistent with that of the 2014 M_w4.9 Milan earthquake, which is also compatible with the regional tectonic stress field and mapped fault distribution (Schoenball & Ellsworth, 2017). The background stressing rate $\dot{\tau}_0$ is based on the geodetic study of strain within the Northern American Plate (Calais et al., 2006). The value of $A\overline{\sigma}$ is set following that proposed by Segall and Lu (2015). The model parameters are provided in Table S2.

3.3. Earthquake Magnitude-Time Simulation

Combining the seismicity rate model and Gutenburg-Richter law, we simulate an earthquake magnitude-time distribution over a particular area and then compare it with observations. The earthquake count per unit area, per unit time, t, per unit magnitude, M, at a specific location $\boldsymbol{x}$ is given by

$$R(\boldsymbol{x}, t, M) = \ln(10)k(\boldsymbol{x})b10^{-bM}R(\boldsymbol{x}, t), \tag{2}$$

where a and b are two parameters associated with the Gutenberg-Richter frequency-magnitude distribution and $k(x)$ is the background seismicity rate defined as $\frac{10^a}{S \times t}$, where S is area. Here, a is location dependent, and we assume spatially constant b value, which is set to 0.93, supported by declustered seismic catalog of the study area (Figure S2). The total number of earthquakes per unit time per unit magnitude is given by integrating over area, S:

$$R(t, M) = \int_S R(\boldsymbol{x}, t, M)d\boldsymbol{x}. \tag{3}$$

Next, we simulate the magnitude-time distribution governed by the function $R(t,M)$. To this end, we discretize the interval, t, into N_t bins of length Δt. We also define the minimum and maximum magnitudes of M_{min}

and M_{max} to mimic a probability distribution. We set M_{min} to 0 and M_{max} to 10 and for each period $[t_i\ t_{i+1}]$, we calculate the total number of earthquakes:

$$N(t_i) = \int_{M_{min}}^{M_{max}} \int_{t_i}^{t_{i+1}} R(t,M)dtdM. \quad (4)$$

We next define a cumulative probability distribution as a function of earthquake magnitude:

$$P(M;t_i) = 1 - \frac{\int_{M}^{M_{max}} \int_{t_i}^{t_{i+1}} R(t,M)dtdM}{\int_{M_{min}}^{M_{max}} \int_{t_i}^{t_{i+1}} R(t,M)dtdM}. \quad (5)$$

We randomly sample this distribution over each interval $[t_i\ t_{i+1}]$ for $N(t_i)$ earthquakes and iterate over the entire observation period to determine the magnitude-time distribution.

4. Results

4.1. Hydromechanical Modeling and Seismicity Rate

We use the records of saltwater injection volume at 668 wells within western Oklahoma and southern Kansas as input to the poroelastic model. We simulate the spatial and temporal evolution of pore pressure and poroelastic stresses for the period 2010–2018. The obtained pore pressure and poroelastic stress models are then used to calculate the time series of changes in the Coulomb failure stress. Next, we apply the rate-and-state-dependent earthquake nucleation model (equation (1)) to estimate the time-dependent seismicity rate changes. The model parameters are listed in Tables S1 and S2. Figures 1d–1f show the cumulative changes in pore pressure, poroelastic stresses, and Coulomb failure stress within the combined area of western Oklahoma and southern Kansas during 2010–2018. The snapshots of annual changes are shown in Figure S5. They show an increasing rate that peaks in 2017, followed by a decaying trend (Figure S6). The contribution of pore pressure change dominates the change of Coulomb failure stress. Also, two Class I wells in the study area (Figure 1a) measure the well-bottom pore pressure (Ansari et al., 2019), which can be used to validate the simulated pore pressure changes. We find a reasonable agreement at well KS-01-077-002 (Figure S7a). However, at well KS-01-173-002 (Figure S7b), the magnitude of simulated pore pressure change is about eight times smaller than that observed. These observations are further discussed in section 5.1. The computed seismicity rate, informed by the Coulomb stressing rate (equation (1)), peaks in mid-2015 (Figures S5 and S6), consistent with the temporal pattern of injection volume (Figure 1b). The seismicity rate snapshots show outward propagation with a decreasing amplitude following large injection rate reduction at high-volume wells.

4.2. Calibration of *k* Value

As seen in Figure 2a, there is a correlation between the location of observed seismicity and that predicted from the seismicity rate model. However, there are zones with a predicted seismicity rate increase but no observed seismicity. To simulate an earthquake catalog, our model requires an estimate of background seismicity rate and predicted seismicity rate change. For the study area, we can assume that the background stressing rate is uniform (Levandowski et al., 2018). Therefore, we suggest that the apparent discrepancy between the simulated relative seismicity rate and observed seismicity is due to spatially variable background seismicity. We can use this discrepancy to estimate the spatially variable k value across the study region, mapped on to the grid used for hydromechanical modeling (section 3.1). We consider the area within a 10-km radius from the center point of each grid cell and compare the number of observed and simulated earthquakes. We assume an unknown k for each circular zone and integrate the right side of equation (2) over its area and the entire observation period of 2010–2018 for magnitudes larger than M2.0, namely, the magnitude completeness of seismic catalog (see Figure S2). This operation ensures that the simulated relative earthquake rate times the unknown k equals the number of observed earthquakes and thus the k value can be estimated for that zone. Figure 2b shows the spatial distribution of the log-transformed k value, which can be used to simulate the earthquake magnitude-time distribution.

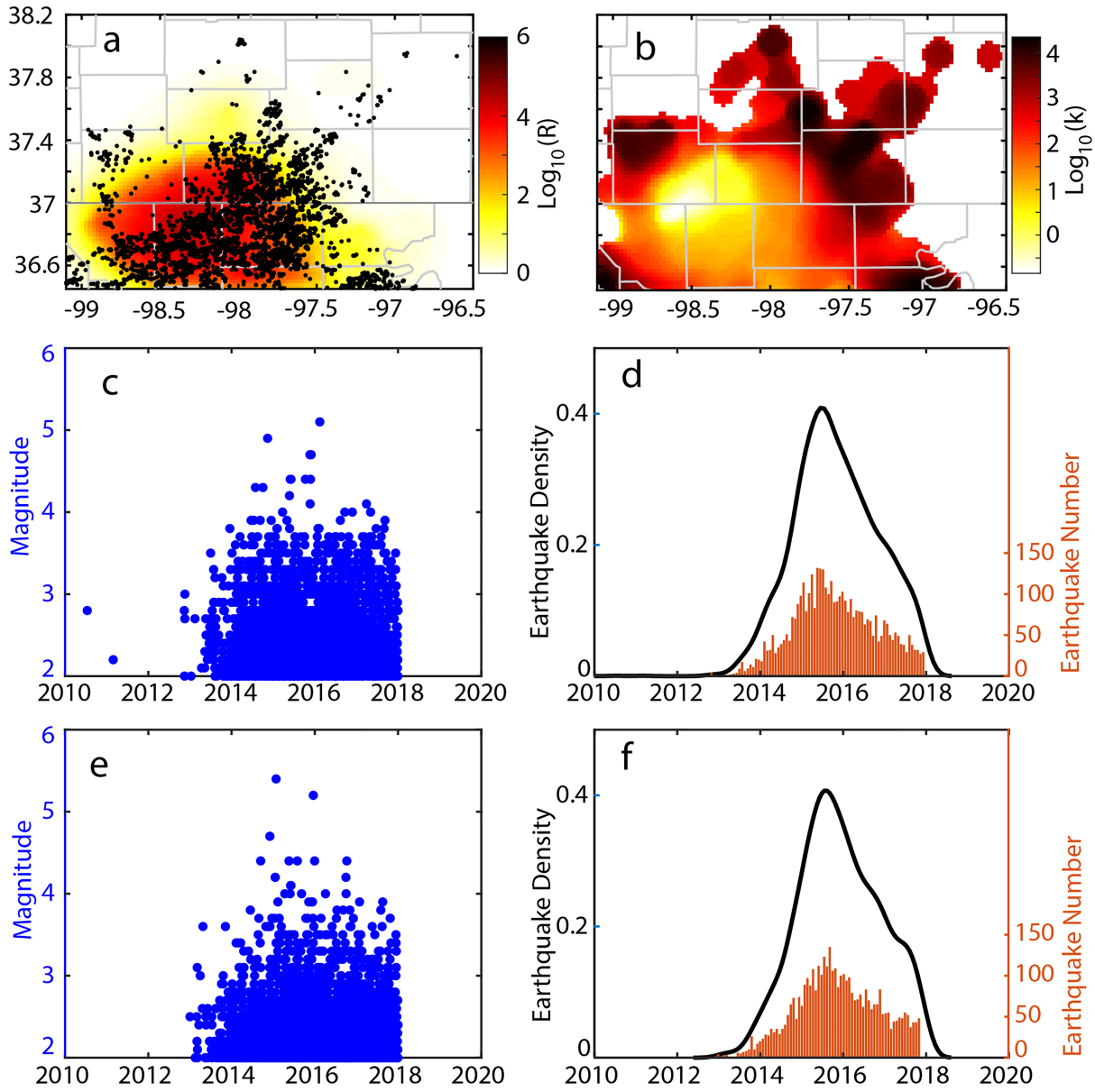

Figure 2. (a) Spatial distribution of observed declustered M2+ earthquakes and temporally average simulated relative seismicity rate for western Oklahoma and southern Kansas. (b) *k*-value distribution obtained by comparing the observed and simulated seismicity rate for western Oklahoma and southern Kansas. (c, e) The observed (panel c) and simulated (panel e) earthquake magnitude-time distributions for the combined area. (d, f) The observed (panel d) and simulated (panel f) earthquake histogram and earthquake count probability density for the combined area. The black curves are probability densities of earthquake number calculated from the earthquake histograms.

4.3. Earthquake Magnitude-Time Distribution

The Gutenberg-Richter law that characterizes background seismicity before fluid injection and the relative seismicity rate change obtained from hydromechanical simulations allow us to simulate the earthquake magnitude-time distribution. In addition to induced earthquake frequency, our method (see section 3.3) can reproduce the time dependence of earthquake magnitude, which is the starting point for time-varying induced earthquake hazard assessment. Figures 2c and 2e show the observed earthquake-time distribution and that simulated using the distributed *k* values and relative seismicity rate. The temporal evolution of seismicity in terms of earthquake magnitude and frequency is reproduced (Figures 2c–2f), and the total number of earthquakes is similar. A peak in 2015 characterizes both observed and simulated magnitude-time distributions.

5. Discussion

To assess future seismic hazard, we need to understand the sensitivity of our results to model parameters, evaluate the role of distant injection, and compute the expected magnitude of induced earthquakes. Seismic hazard is a forecast of seismic ground shaking intensity at a specified site during an interval of time, which is linked to earthquake probability and ground motion equations (Baker, 2015). Thus, earthquake probability can be a first-order manifestation of seismic hazard, whose conversion to the ground motion probability is straightforward (Baker, 2015).

5.1. Model Uncertainties

Although our model successfully reproduces the time series of pore pressure change during 2010–2018 at Class I well KS-01-077-002 (Figure S7a), the simulated pore pressure change at Class I well KS-01-173-002 is eight times smaller than that observed (Figure S7b). This underestimate can be due to several factors. In addition to monitoring well-bottom pressure, Class I wells also inject fluid into the Arbuckle formation, which can locally increase pore pressure. This effect is more significant at KS-01-173-002 because the injection volume at KS-01-173-002 is one order of magnitude larger than that at KS-01-077-002 (Ansari et al., 2019). However, the depths of Class I wells are not available, which prevent us from including Class I well injection in the hydromechanical simulation. Also, the simulated pore pressure change from our model is at the Arbuckle-basement interface, while Class I well-bottom pressure record can have shallower depths. The different simulation and observation depths can result in a significant difference in pore pressure because pore pressure decays exponentially in space (Segall & Lu, 2015). To assess this effect, we implemented simulations using the published injection volumes at KS-01-173-002 during 2010–2016 (Ansari et al., 2019), assuming a range of well depths. Figure S8 shows that the well-bottom pressure is larger than that at the Arbuckle-basement interface if the well depth is shallower. However, the observed well-bottom pressure falls within the range of simulated well-bottom pressure (Figures S7 and S8), suggesting that the observed well-bottom pressure is largely due to Class I well injection at KS-01-173-002.

Besides heterogeneous background seismic productivity, the other possibilities to explain the apparent discrepancy between simulated and observed seismicity rate include heterogeneous background tectonic stress and diffusivity. However, the regional stress map indicates that tectonic stress is relatively uniform within our study area (Levandowski et al., 2018). While diffusivity is likely not uniform (Ansari et al., 2019; Zhai et al., 2019), it has only a second-order effect because injection wells are located within the zone with no observed seismicity (Figures 1a and S1), and the bottom of injection wells is close to the Arbuckle-basement interface (Figure S4).

The triggering mechanisms for injection-induced seismicity include pore pressure diffusion, poroelastic stresses, and static Coulomb stress transfer. In this work, we only focus on pore pressure and poroelastic stresses and decluster the earthquake catalog to eliminate earthquake sequences. Other studies suggest that earthquakes can be caused in part by previous induced events or aseismic slip through static Coulomb stress transfer (Bhattacharya & Viesca, 2019; Brown & Ge, 2018; Qin et al., 2018) in addition to the direct effect of fluid injection. More effort is needed to incorporate the static Coulomb stress transfer into seismicity rate forecasting.

5.2. The Effect of Cross-Border Injection

Many induced earthquakes occur near injection wells, and the seismicity is preceded by high-volume fluid injection over months to years. However, some studies also show that earthquakes occur beyond zones of high-volume injection, suggesting mechanical interaction between distant injection operations and seismicity. Keranen et al. (2014) show that pore pressure changes caused by high-volume injections near Oklahoma City can propagate ~35 km to explain the 2011 Jones earthquake swarm. The Fairview earthquake sequence may have been triggered by clustered fluid injection 40 km away near the Oklahoma-Kansas border; however, instead of pore pressure propagation, poroelastic stresses were proposed to be the driver of the seismicity (Goebel et al., 2017). Regardless of the mechanisms, these observations indicate that the stress field perturbation due to fluid injection can reach as far as 40 km. The present study provides another example of the far-reaching impact of fluid injection in south-central Kansas that possibly acts over distances of up to 90 km (Peterie et al., 2018). Although geospatial analysis of fluid injection and seismicity in Oklahoma implies that this far-reaching triggering is possible, the

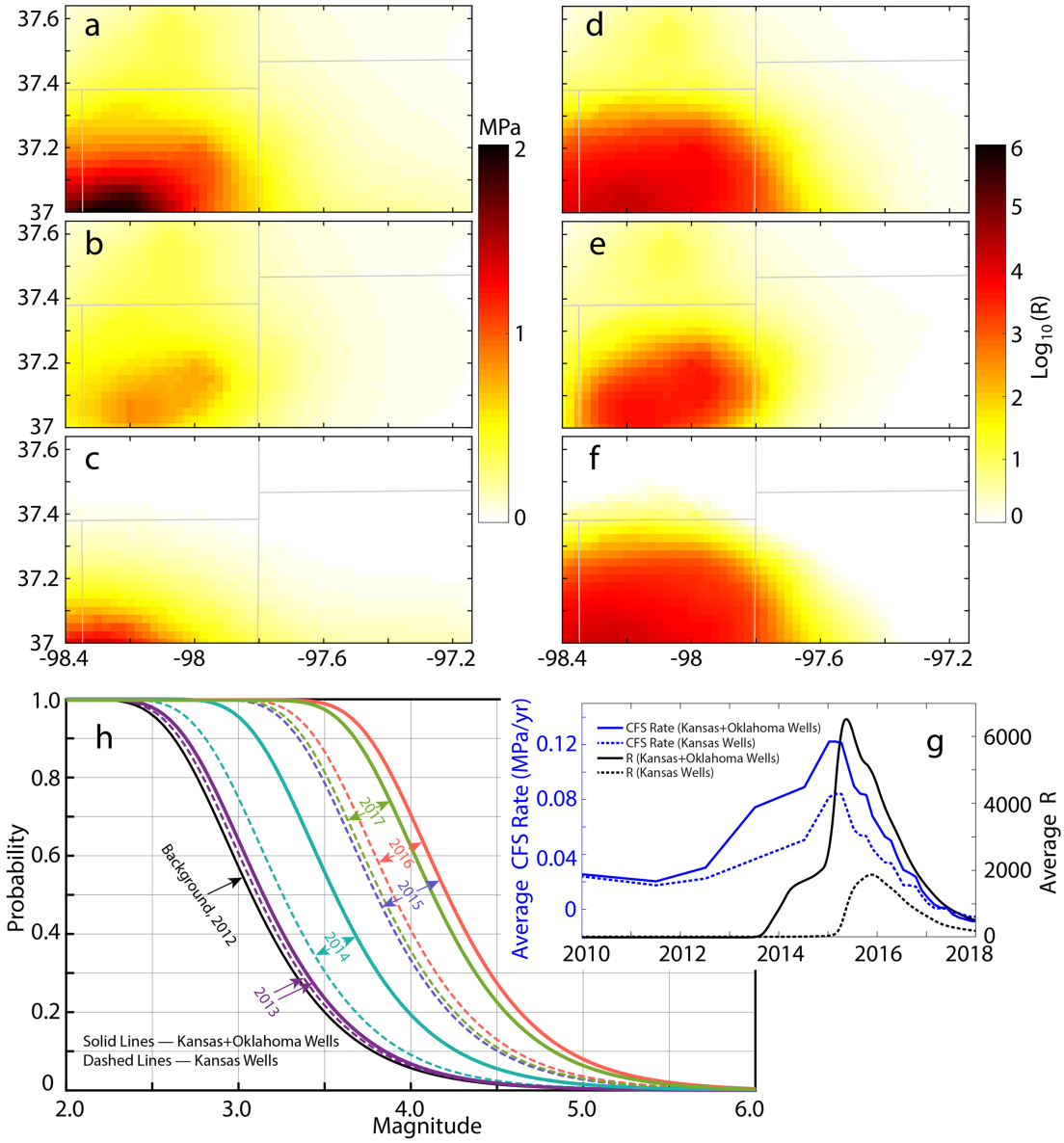

Figure 3. (a) Cumulative Coulomb failure stress during 2010–2018 in south-central Kansas due to both western Oklahoma and southern Kansas wells. (b) Same as panel a but only considering Kansas wells. (c) The difference between that shown in panels a and b. (d, e) The distribution of average simulated seismicity rate in logarithmic scale during 2010–2018 corresponding with stress change shown in panels a and b, respectively. (f) The difference of *R* between panels d and e. (g) Time series of average Coulomb failure stressing rate and seismicity rate within south-central Kansas with and without western Oklahoma wells. The stressing rate prior to 2015 is downsampled to an annual average. (h) Annual earthquake magnitude exceedance probability in south-central Kansas with (solid lines) and without (dashed lines) western Oklahoma wells. Note that the 2015 and 2016 solid curves overlap.

importance of geological complexities are not considered (Pollyea et al., 2018). The northward propagation of seismicity in Kansas indicates that fluid diffusion from the south is the main driver (Peterie et al., 2018). Our unified hydromechanical model allows us to examine the far-reaching effect of injection in Western Oklahoma on the stress field (Figures 3a–3c) and the associated seismicity rate (Figures 3d–3f) in south-central Kansas. The western Oklahoma wells can affect spatial patterns of Coulomb stress change and seismicity rate distribution with the highest effect in the southern part of south-central Kansas that diminishes northward (Figures 3c and 3f). Including western Oklahoma wells, in addition to southern Kansas wells, increases Coulomb stressing rate by a factor of 1.5 in south-central Kansas, which advances the seismicity increases by 1–2 years and amplifies seismicity rate by approximately threefold (Figure 3g).

5.3. Probabilistic Seismic Hazard

A crucial component of probabilistic seismic hazard analysis is an estimate of the spatiotemporal distribution of seismicity (Cornell, 1968). Generally, the seismicity distribution is modeled through smoothing the recorded earthquakes to obtain a grid of Gutenberg-Richter sources. Applying probabilistic seismic hazard analysis to estimate future seismic hazard due to anthropogenic processes, such as injection-induced earthquakes (Petersen et al., 2016; Petersen et al., 2017; Petersen et al., 2018), is challenging because injection operations and thus subsequent seismicity show substantial spatial and temporal variations, which cannot be captured robustly using conventional methods of spatial smoothing and temporal extrapolation.

Our method considers the physical processes of fluid diffusion and rate-and-state earthquake nucleation to simulate relative seismicity rate, which is scaled with background seismicity rate to obtain absolute seismicity rate. Due to limited seismic activity before 2012, estimating the k-value distribution, which characterizes the background seismicity rate distribution, is not possible. However, fluid injection operations can relate background seismicity to observations through physical models, allowing us to estimate background seismicity indirectly. Assuming that the background tectonic loading, and thus the background seismicity rate, is steady, then we can reasonably use the mapped k value to forecast expected future earthquake probability due to stress evolution under specifically designed injection scenarios. For combined western Oklahoma and southern Kansas, the injection data are collected through December 2017. Therefore, we focus on the retrospective investigation of earthquake probability until the end of 2017. We estimate earthquake magnitude exceedance probability ($P_{\geq M}$) considering the Poisson process:

$$P_{\geq M} = 1 - \exp(N_{\geq M}), \tag{6}$$

where $N_{\geq M}$ is the estimated number of earthquakes with magnitude larger than or equal to M through the integration of equation (2). The value of exceedance probability depends on time and space scales considered. Here, we show the annual earthquake exceedance probability over the area of south-central Kansas (Figure 3h). The annual exceedance probability is time dependent, and the annual probability for exceeding M4 increases from 7% in 2013 to 70% in 2015 and 2016, followed by a decrease to 63% in 2017. Also, we calculated the exceedance probability by ignoring Oklahoma injection, which results in a consistent probability decrease for each year with a maximum reduction of 36 % in 2015 for exceeding M4.

6. Conclusions

We construct a unified hydromechanical and induced seismicity rate model in the combined area of western Oklahoma and southern Kansas. This physics-based model, combined with seismic observations, can be used to map background earthquake productivity. It also allows us to examine and quantify the long-distance mechanical interactions between injection practices and induced seismicity. We demonstrate that injection in Oklahoma can change the spatiotemporal patterns and amplitudes of Coulomb failure stress and seismicity rate in Kansas. Ignoring these interactions results in systematic underestimates of annual earthquake magnitude exceedance probability in Kansas. These results highlight that the far-reaching effect due to fluid diffusion is crucial in understanding induced earthquake nucleation and assessing the associated seismic hazard. Since fluid pressure and stress changes do not respect state or county borders, regulation and management should be coordinated across agencies to mitigate induced seismicity.

Acknowledgments
We thank the Oklahoma Corporation Commission and the Kansas Corporation Commission for making the injection data publicly available, which can be downloaded at http://www.occeweb.com/OG/ogdatafiles2.htm and http://www.kgs.ku.edu/Magellan/Qualified/fluid.html, respectively. Earthquake catalogs archived by Oklahoma geological survey and Kansas geological survey are accessible through http://www.ou.edu/ogs/research/earthquakes/catalogs and http://www.kgs.ku.edu/Geophysics/Earthquakes/data.html, respectively. G. Z., M. S., and M. M. are supported by Department of Energy Grant DE-SC0019307. We thank the reviewers for constructive suggestions.

References

Ake, J., Mahrer, K., O'Connell, D., & Block, L. (2005). Deep-injection and closely monitored induced seismicity at Paradox Valley, Colorado. *Bulletin of the Seismological Society of America*, *95*(2), 664–683.

Al-Ismail, F., Ellsworth, W. L., & Beroza, G. C. (2019), Empirical and synthetic approaches to the calibration of the local magnitude scale, M_L, in southern Kansas, Paper Presented at AGU Fall Meeting 2019, AGU.

Ansari, E., Bidgoli, T., & Hollenbach, A. (2019). Accelerated fill-up of the Arbuckle Group aquifer and links to US midcontinent seismicity. *Journal of Geophysical Research: Solid Earth*, *124*, 2670–2683. https://doi.org/10.1029/2018JB016926

Baker, J. (2015), An introduction to probabilistic seismic hazard analysis (PSHA), White Paper, Version 2.1, 77 pp, edited.

Barbour, A. J., Xue, L., Roeloffs, E., & Rubinstein, J. L. (2019). Leakage and increasing fluid pressure detected in Oklahoma's wastewater disposal reservoir. *Journal of Geophysical Research: Solid Earth*, *124*, 2896–2919. https://doi.org/10.1029/2019JB017327

Bhattacharya, P., & Viesca, R. C. (2019). Fluid-induced aseismic fault slip outpaces pore-fluid migration. *Science*, *364*(6439), 464–468. https://doi.org/10.1126/science.aaw7354

Block, L. V., Wood, C. K., Yeck, W. L., & King, V. M. (2014). The 24 January 2013 ML 4.4 earthquake near Paradox, Colorado, and its relation to deep well injection. *Seismological Research Letters*, *85*(3), 609–624. https://doi.org/10.1785/0220130188

Brown, M. R., & Ge, S. (2018). Small earthquakes matter in injection-induced seismicity. *Geophysical Research Letters*, *45*, 5445–5453. https://doi.org/10.1029/2018GL077472

Calais, E., Han, J. Y., DeMets, C., & Nocquet, J. M. (2006). Deformation of the North American plate interior from a decade of continuous GPS measurements. *Journal of Geophysical Research*, *111*, B06402. https://doi.org/10.1029/2005jb004253

Campbell, J. A., & J. L. Weber (2006), Wells drilled to basement in Oklahoma.

Chang, K. W., & Yoon, H. (2018). 3-D Modeling of induced seismicity along multiple faults: Magnitude, rate, and location in a poroelasticity system. *Journal of Geophysical Research: Solid Earth*, *123*, 9866–9883. https://doi.org/10.1029/2018JB016446

Chen, C. (2016). Comprehensive analysis of Oklahoma earthquakes: From earthquake monitoring to 3D tomography and relocation.

Choy, G. L., Rubinstein, J. L., Yeck, W. L., McNamara, D. E., Mueller, C. S., & Boyd, O. S. (2016). A Rare Moderate- Sized (M-w 4.9) Earthquake in Kansas: Rupture process of the Milan, Kansas, earthquake of 12 November 2014 and its relationship to fluid injection. *Seismological Research Letters*, *87*(6), 1433–1441. https://doi.org/10.1785/0220160100

Christensen, N. I. (1996). Poisson's ratio and crustal seismology. *Journal of Geophysical Research*, *101*, 3139–3156.

Cornell, C. A. (1968). Engineering seismic risk analysis. *Bulletin of the Seismological Society of America*, *58*, 1583–1606.

Dieterich, J. H. (1994). A constitutive law for rate of earthquake production and its application to earthquake clustering. *Journal of Geophysical Research*, *99*, 2601–2618.

Ellsworth, W. L. (2013). Injection-induced earthquakes. *Science*, *341*. https://doi.org/10.1126/science.1225942

Fan, Z., Eichhubl, P., & Gale, J. F. (2016). Geomechanical analysis of fluid injection and seismic fault slip for the Mw 4. 8 Timpson, Texas, earthquake sequence. *Journal of Geophysical Research: Solid Earth*, *121*, 2798–2812. https://doi.org/10.1002/2016JB012821

Franseen, E. K., & Byrnes, A. P. (2012). Arbuckle Group platform strata in Kansas: A synthesis. In J. Derby, R. Fritz, S. Longacre, W. Morgan, & C. Sternbach (Eds.), *Great American carbonate bank: The geology and economic resources of the Cambrian—Ordovician Sauk megasequence of Laurentia*, *American Association of Petroleum Geologists* (Chap. 24, pp. 1031–1047). Tulsa, Oklahoma: Co-published by AAPG and Shell. https://doi.org/10.1306/13331528m981452

Franseen, E. K., Byrnes, A. P., Cansler, J. R., Steinhauff, D. M., & Carr, T. R. (2004). The geology of Kansas Arbuckle Group. *Kansas Geological Survey Bulletin*, *250*, 43.

Frohlich, C. (2012). Two-year survey comparing earthquake activity and injection-well locations in the Barnett Shale, Texas. *Proceedings of the National Academy of Sciences*, *109*(35), 13,934–13,938.

Goebel, T. H. W., Hosseini, S. M., Cappa, F., Hauksson, E., Ampuero, J. P., Aminzadeh, F., & Saleeby, J. B. (2016). Wastewater disposal and earthquake swarm activity at the southern end of the Central Valley, California. *Geophysical Research Letters*, *43*, 1092–1099. https://doi.org/10.1002/2015gl066948

Goebel, T. H. W., Weingarten, M., Chen, X., Haffener, J., & Brodsky, E. E. (2017). The 2016 Mw5.1 Fairview, Oklahoma earthquakes: Evidence for long-range poroelastic triggering at >40 km from fluid disposal wells. *Earth and Planetary Science Letters*, *472*, 50–61. https://doi.org/10.1016/j.epsl.2017.05.011

Healy, J. H., Rubey, W. W., Griggs, D. T., & Raleigh, C. B. (1968). The Denver earthquakes. *Science*, *161*(3848), 1301–1310. https://doi.org/10.1126/science.161.3848.1301

Hearn, E. H., Koltermann, C., & Rubinstein, J. L. (2018). Numerical models of pore pressure and stress changes along basement faults due to wastewater injection: Applications to the 2014 Milan, Kansas earthquake. *Geochemistry, Geophysics, Geosystems*, *19*, 1178–1198. https://doi.org/10.1002/2017GC007194

Heimisson, E. R., & Segall, P. (2018). Constitutive law for earthquake production based on rate-and-state friction: Dieterich 1994 revisited. *Journal of Geophysical Research: Solid Earth*, *123*, 4141–4156. https://doi.org/10.1029/2018JB015656

Hincks, T., Aspinall, W., Cooke, R., & Gernon, T. (2018). Oklahoma's induced seismicity strongly linked to wastewater injection depth. *Science*, *359*(6381), 1251–1255. https://doi.org/10.1126/science.aap7911

Horton, S. (2012). Disposal of hydrofracking waste fluid by injection into subsurface aquifers triggers earthquake swarm in Central Arkansas with potential for damaging earthquake. *Seismological Research Letters*, *83*(2), 250–260. https://doi.org/10.1785/gssrl.83.2.250

Keranen, K. M., Weingarten, M., Abers, G. A., Bekins, B. A., & Ge, S. (2014). Sharp increase in central Oklahoma seismicity since 2008 induced by massive wastewater injection. *Science*, *345*(6195), 448–451. https://doi.org/10.1126/science.1255802

Kim, W.-Y. (2013). Induced seismicity associated with fluid injection into a deep well in Youngstown, Ohio. *Journal of Geophysical Research: Solid Earth*, *118*, 3506–3518. https://doi.org/10.1002/jgrb.50247

Kolawole, F., Johnston, C. S., Morgan, C. B., Chang, J. C., Marfurt, K. J., Lockner, D. A., et al. (2019). The susceptibility of Oklahoma's basement to seismic reactivation. *Nature Geoscience*, *12*(10), 839–844. https://doi.org/10.1038/s41561-019-0440-5

Kroll, K. A., Cochran, E. S., & Murray, K. E. (2017). Poroelastic properties of the Arbuckle Group in Oklahoma derived from well fluid level response to the 3 September 2016 M w 5.8 Pawnee and 7 November 2016 M w 5.0 Cushing earthquakes. *Seismological Research Letters*, *88*(4), 963–970.

Levandowski, W., Herrmann, R. B., Briggs, R., Boyd, O., & Gold, R. (2018). An updated stress map of the continental United States reveals heterogeneous intraplate stress. *Nature Geoscience*, *11*(6), 433.

Perilla-Castillo, P. (2017). *Rock properties derived from analysis of earth tide strain observed in continuous pressure monitoring of the Arbuckle Group of Oklahoma*. Norman, Oklahoma: University of Oklahoma.

Peterie, S. L., Miller, R. D., Intfen, J. W., & Gonzales, J. B. (2018). Earthquakes in Kansas induced by extremely far-field pressure diffusion. *Geophysical Research Letters*, *45*, 1395–1401. https://doi.org/10.1002/2017GL076334

Petersen, M. D., Mueller, C. S., Moschetti, M. P., Hoover, S. M., Llenos, A. L., Ellsworth, W. L., et al. (2016), 2016 one-year seismic hazard forecast for the central and eastern United States from induced and natural earthquakes Rep. 2331-1258, US Geological Survey.

Petersen, M. D., Mueller, C. S., Moschetti, M. P., Hoover, S. M., Rukstales, K. S., McNamara, D. E., et al. (2018). 2018 One-year seismic hazard forecast for the central and eastern United States from induced and natural earthquakes. *Seismological Research Letters*, *89*(3), 1049–1061.

Petersen, M. D., Mueller, C. S., Moschetti, M. P., Hoover, S. M., Shumway, A. M., McNamara, D. E., et al. (2017). 2017 one-year seismic-hazard forecast for the Central and Eastern United States from induced and natural earthquakes. *Seismological Research Letters*, *88*(3), 772–783.

Pollyea, R. M., Mohammadi, N., Taylor, J. E., & Chapman, M. C. (2018). Geospatial analysis of Oklahoma (USA) earthquakes (2011–2016): Quantifying the limits of regional-scale earthquake mitigation measures. *Geology*, *46*(3), 215–218.

Qin, Y., Chen, X., Carpenter, B. M., & Kolawole, F. (2018). Coulomb stress transfer influences fault reactivation in areas of wastewater injection. *Geophysical Research Letters*, *45*, 11,059–11,067. https://doi.org/10.1029/2018GL079713

Raleigh, C. B., Healy, J. H., & Bredehoeft, J. D. (1976). An experiment in earthquake control at Rangely. *Colorado*, *191*(4233), 1230–1237. https://doi.org/10.1126/science.191.4233.1230

Reasenberg, P. (1985). Second-order moment of central California seismicity, 1969–1982. *Journal of Geophysical Research*, *90*(B7), 5479–5495.

Rubinstein, J. L., Ellsworth, W. L., & Dougherty, S. L. (2018). The 2013–2016 induced earthquakes in Harper and Sumner counties, Southern Kansas. *Bulletin of the Seismological Society of America*, *108*(2), 674–689.

Rubinstein, J. L., Ellsworth, W. L., McGarr, A., & Benz, H. M. (2014). The 2001-present induced earthquake sequence in the Raton Basin of Northern New Mexico and Southern Colorado. *Bulletin of the Seismological Society of America*, *104*(5), 2162–2181. https://doi.org/10.1785/0120140009

Rubinstein, J. L., & Mahani, A. B. (2015). Myths and facts on wastewater injection, hydraulic fracturing, enhanced oil recovery, and induced seismicity. *Seismological Research Letters*, *86*(4), 1060–1067. https://doi.org/10.1785/0220150067

Schoenball, M., & Ellsworth, W. L. (2017). Waveform-relocated earthquake catalog for Oklahoma and southern Kansas illuminates the regional fault network. *Seismological Research Letters*, *88*(5), 1252–1258.

Scibek, J., Gleeson, T., & McKenzie, J. (2016). The biases and trends in fault zone hydrogeology conceptual models: Global compilation and categorical data analysis. *Geofluids*, *16*(4), 782–798.

Segall, P., & Lu, S. (2015). Injection-induced seismicity: Poroelastic and earthquake nucleation effects. *Journal of Geophysical Research: Solid Earth*, *120*, 5082–5103. https://doi.org/10.1002/2015jb012060

Shirzaei, M., Ellsworth, W. L., Tiampo, K. F., González, P. J., & Manga, M. (2016). Surface uplift and time-dependent seismic hazard due to fluid injection in eastern Texas. *Science*, *353*(6306), 1416–1419. https://doi.org/10.1126/science.aag0262

Shirzaei, M., Manga, M., & Zhai, G. (2019). Hydraulic properties of injection formations constrained by surface deformation. *Earth and Planetary Science Letters*, *515*, 125–134. https://doi.org/10.1016/j.epsl.2019.03.025

Wang, H. F. (2000). *Theory of linear poroelasticity with applications to geomechanics and hydrogeology*, (p. 276). Princeton, N.J.: Princeton Univ. Press.

Wang, R. J., & Kümpel, H. J. (2003). Poroelasticity: Efficient modeling of strongly coupled, slow deformation processes in a multilayered half-space. *Geophysics*, *68*(2), 705–717. https://doi.org/10.1190/1.1567241

Yeck, W. L., Block, L. V., Wood, C. K., & King, V. M. (2014). Maximum magnitude estimations of induced earthquakes at Paradox Valley, Colorado, from cumulative injection volume and geometry of seismicity clusters. *Geophysical Journal International*, *200*(1), 322–336.

Yeck, W. L., Sheehan, A., Benz, H. M., Weingarten, M., & Nakai, J. (2016). Rapid response, monitoring, and mitigation of induced seismicity near Greeley, Colorado. *Seismological Research Letters*, *87*(4), 837–847.

Zhai, G., & Shirzaei, M. (2018). Fluid injection and time-dependent seismic hazard in the Barnett Shale, Texas. *Geophysical Research Letters*, *45*, 4743–4753. https://doi.org/10.1029/2018GL077696

Zhai, G., Shirzaei, M., Manga, M., & Chen, X. (2019). Pore-pressure diffusion, enhanced by poroelastic stresses, controls induced seismicity in Oklahoma. *Proceedings of the National Academy of Sciences*, *116*(33), 16,228–16,233. https://doi.org/10.1073/pnas.1819225116